

THE PENNSYLVANIA STATE UNIVERSITY  
SCHREYER HONORS COLLEGE

DEPARTMENT OF ASTRONOMY AND ASTROPHYSICS

TEMPERATURE SIMULATION AND CALCULATION FOR THE ANTIMATTER  
EXPERIMENT: GRAVITY, INTERFEROMETRY, AND SPECTROSCOPY

STEPHANIE BROWN  
SPRING 2018

A thesis  
submitted in partial fulfillment  
of the requirements  
for a baccalaureate degree  
in Astronomy and Astrophysics  
with honors in Astronomy and Astrophysics

Reviewed and approved\* by the following:

Miguel Mostafa  
Professor of Physics  
Thesis Supervisor

Christopher Palma  
Professor of Astronomy and Astrophysics  
Honors Adviser

\*Signatures are on file in the Schreyer Honors College.

# Abstract

An important aspect of an antimatter plasma is the temperature, and it is critical to the success of the  $AE\bar{g}IS$  experiment that we are able to accurately determine the temperature of our plasma and hence the effectiveness of our cooling systems. The goal of the  $AE\bar{g}IS$  experiment is to measure the acceleration due to gravity on antihydrogen atoms. The atoms will be allowed to free fall. The slower the particles tangential velocity, the larger the vertical deflection will be. Since our detectors have a finite spacial resolution, we must require that the temperature of the particles is below a threshold ( $\sim \mu\text{K}$ ). This thesis discusses a simulation that mimics the measurement. The temperature is calculated using the Maxwell-Boltzmann equation to relate kinetic energy to temperature. A potential well contains the particles. The potential well is slowly lowered so that small numbers of particles escape at a time. Since we know particle number as a function of energy, we can determine the temperature of the ensemble. We treat the particles classically and neglect quantum effects. We only extract the first 1% of the particles in the simulation as, in the actual experiment, we want to remove only the high energy tail of the particles. Doing this will minimize the effects of space charge and evaporative cooling. We use this simulation to examine the effects of different parameters such as temperature, particle number, and ramping speed on the measurement. In addition, we will examine the fit used to retrieve the temperature and the error inherent in the calculation, which contains some approximations.

# Table of Contents

<b>List of Figures</b>	<b>iii</b>
<b>List of Tables</b>	<b>v</b>
<b>Acknowledgements</b>	<b>vi</b>
<b>1 Introduction</b>	<b>1</b>
1.1 Antimatter . . . . .	2
1.2 The role of $AE\bar{g}IS$ in the field of antimatter . . . . .	4
1.3 Temperature measurements for $AE\bar{g}IS$ . . . . .	5
1.4 Theoretical Motivation . . . . .	6
<b>2 Hardware for Temperature Calculation with <math>AE\bar{g}IS</math> Apparatus</b>	<b>7</b>
2.1 Introduction and Background . . . . .	8
2.2 Description of the measurement apparatus . . . . .	8
2.2.1 Micro-channel plate detectors . . . . .	8
2.2.2 Phosphor Screen . . . . .	9
2.2.3 Front-end Box . . . . .	10
2.2.4 Field Programable Gate Array . . . . .	10
<b>3 Simulation of Plasma in the <math>AE\bar{g}IS</math> Trap</b>	<b>11</b>
3.1 Introduction and Basic Information . . . . .	12
3.2 Parameter Space Explored . . . . .	13
3.3 Error Analysis and Consistency Checks . . . . .	16
3.4 Limitations on the model . . . . .	20
3.5 Conclusions . . . . .	21
<b>4 Outlook</b>	<b>23</b>
<b>Bibliography</b>	<b>24</b>

# List of Figures

1.1	This image, taken from the AE $\bar{g}$ IS collaboration site [1], shows the star shaped annihilation pattern caused by proton-proton annihilation. . . . .	3
1.2	This is a schematic of a simple Penning-Malmberg trap. This is a trap designed to contain charged plasma. Two end voltages repel the charged particles in the center and an axial magnetic field gives radial confinement. . . . .	4
1.3	This graph demonstrates the distance in the vertical deflection of a proton falling in free fall on earth's surface. The slower the speed, the larger the deflection. Since the trap length is only 0.1 m and the detector resolution is limited, slower speeds are critical to ensure that particle deflection can be measured. . . . .	5
2.1	Diagram of a round MCP detector taken from the Hamamatsu Technical MCP Manual [2]. . . . .	9
2.2	This image shows how the phosphor screen relates to the two-stage MCP detector. The two numbers -2kV and +4kV respectively show the strength of the relative voltage than can be applied. This diagram is taken from the Hamamatsu Technical MCP Manual [2]. . . . .	9
2.3	An example of an analog signal (left) being digitized (right). . . . .	10
3.1	This a sample run, the red line shows the fit to the data. . . . .	13
3.2	These plots have the same input parameters ( $T = 10$ K, $\Delta W = 0.0001$ eV, $\Delta T = 0.001$ K), except for the number of particles. You can see that the calculated temperature is closer to the real value and that the error is smaller for the higher particle number. The fit is shown by the small red line on the peak. . . . .	14
3.3	These graphs show the effects of the values of the potential steps $\Delta W$ and the time steps $\Delta t$ . You see looking from left to right that when you reduce the value of $\Delta W$ and $\Delta t$ by even 1/4 that you have a large change in the accuracy of the measurement. The small red line represents the fit to the 1% particles with the highest energy. . . . .	14
3.4	This image shows the calculated temperature as a function of ramping speed. In this case, the time step was held constant. . . . .	15
3.5	This is the example of a histogram for a ramping speed greater than $1.3 \pm 0.5$ eV/ms. . . . .	15

- 3.6 These figures are zoomed in so that you can see the high end tail of the fit. Note that in the left image, the first bin contains more particles than the second bin. This is because the potential well was set too low. As a result, the exponential fit is negative and gives a negative temperature. The right figure shows that changing the initial voltage changes the output temperature. . . . . 16
- 3.7 This figure shows how noise on the end caps that provide the voltages in the penning trap effect the measurement. . . . . 17
- 3.8 This figure contains four graphs that demonstrate the effect of detection efficiency on the temperature measurement. The two on the top have an initial temperature of 10 K and the bottom have an initial temperature of 20 K. On the left, the detection efficiency is set to 10% and on the right it is set to 100%. These plots demonstrate that the physical limitation of detection efficiency does not significantly affect the measurement. . . . . 18
- 3.9 These are side by side plots where the original function and the approximated function have been used to determine how many particles escaped the trap. There is no visible difference in the two as the relative error is 0.0015% in this case ( $T = 50$  K). . . . . 19
- 3.10 This shows the percent error on the number of escaped particles in a ramping step as a function of the voltage at the end cap. Each line corresponds to a different temperature from 10-100 K in increments of 10. The peak moves right as the temperature increases. However, the error in all cases is less than 0.025%, as you can see in this figure. . . . . 19
- 3.11 The parameters used are as follows: particle number =  $10^5$ , temperature (T) = 20 K, Voltage steps (dW) = 0.001V, time steps (dt) = 0.001 s . . . . . 20
- 3.12 This figure is taken from [3]. This was made using a program known as EQUILSOR, which simulates plasmas. It shows calculation of the total trap depth  $W$  as a function of empty trap well depth  $W + 0$  and density of the plasma  $\rho$  . . . . . 21

# Acknowledgements

This thesis has been a two year journey, and I couldn't have done it alone. I would like to thank Dr. Michael Doser at AĒIS for accepting me onto his team, and (soon to be Dr.) Igmari Tietje for working with me day to day. I'd also like to thank Dr. Miguel Mostafa for being my thesis advisor and being so generous with his time. This work wouldn't have been possible without Steven Goldfarb and the University of Michigan group behind the CERN US Summer Student Program and the CERN Semester Abroad program. My time at CERN was also made possible by the Erickson Discover Grant.

I'd also like to thank my parents for letting their only child live on her own in Switzerland for six months. Thanks to my father, who didn't live to see me come home from CERN, and to my mother, Dr. Keilholtz, who never let me think that women couldn't do science. I am also grateful to my boyfriend and my friends at CERN for making a foreign country feel like home.

Finally I'd like to thank Renata Kopečná, Miguel Angel Quero Corrales, and Dr. Wendy Keilholtz for taking the time to read my thesis and give me feedback.

# **Chapter 1**

## **Introduction**

## 1.1 Antimatter

Physics changed radically at the beginning of the 1900s. In 1900, Max Planck famously published his equation  $E = h\nu$ , saying that light was a quantized particle, but also a wave with a specific frequency. Then, in 1905 and 1915, Albert Einstein published his theories of special and general relativity respectively. Special relativity stated that the speed of light in a vacuum ( $c = 3 \times 10^8$  m/s) is a constant and that nothing can exceed this speed [4]. Werner Heisenberg and Erwin Schrodinger worked separately to come up with mathematical formulations of what is now known as Quantum Mechanics. However, their formulations only applied to particles moving at speeds much less than the speed of light. In 1928, Paul Dirac published an equation that combined quantum mechanics and special relativity. However, there was something unusual in his equation; Dirac's equation had two solutions. This meant that for every particle there should be an antiparticle with negative energy or a particle that moves backwards in time. However, it is understood that particles can only have positive energy and time only moves forward. For this reason, Dirac proposed that for every particle there was an antiparticle that was the same mass as the particle, but it had the opposite electric charge and spin. Thus an antielectron would have the same mass as an electron, but a charge of  $+e$  instead of  $-e$  [5]. Looking at this solution, Dirac proposed a universe made of this new form of matter.

After Dirac predicted the antielectron, scientists began to search for this new type of particle. In 1932, Carl Anderson discovered a new particle in his cloud chamber. The cloud chamber is designed to study cosmic rays: the highest energy particles available in the 1930s. The particle had the same mass as an electron, but a positive charge. It was more than a year before he recognized that the particle, which he called a positron, was an antielectron [6]. Occhialini and Blackett confirmed his discovery. However, no one detected positrons with a terrestrial source. After finding the positron, people turned to hunt for the antiproton. It was more than 20 years before any success. The antiproton is three orders of magnitude more massive than the positron, for this reason it requires even higher energy to be detected.

In 1930, Ernest Lawrence invented the cyclotron. This device could accelerate protons to energies of several MeV. This kicked off the era of high energy physics. More than twenty years later, Lawrence built the Bevatron at Berkeley. This device could accelerate particles up to several GeV, which was referred to as BeV (billion electron volts) at the time. This machine could collide protons at an energy of 6.2 GeV. This is the energy at which he expected to find antiprotons. Scientists Emilio Segré and Owen Chamberlain were in charge of building a detector for the antiproton. The detector needed to separate the antiproton out from all the other particles produced in the collision in about ten millionths of a second before the antiproton collided with a proton and disappeared [7]. Since mass and charge are the defining characteristics of the antiproton, they needed to find a way to determine these two properties. They decided to measure momentum and velocity. They used a series of quadrupole magnets to determine the momentum of the particle. This system allowed only negatively charged particles with a certain momentum to pass. Positive particles were repelled by the magnets. Particles that had too large or too small momentum would impinge on the magnets and not escape to the detector. To determine the velocity they used two scintillators separated by 12 meters. Pions had similar momentum and could make it past the magnets, but they would traverse the 12 meters at a different speed. As a back up, they brought in two Cherenkov detectors. One was a liquid fluorocarbon detector that would measure particles moving

faster than antiprotons and one was quartz and it detected particles moving at the anticipated speed of the antiproton. As a final way to avoid false detections, they added photo emulsion plates that would display the characteristic star pattern from proton-antiproton annihilation (Shown in Figure 1.1). Segré and Chamberlain detected 60 antiprotons in their experiment [8]. They published their findings in 1955. One year later another team, (Bruce Cork, Glen R. Lambertson, Oreste Piccioni, and William A. Wenzel) discovered the antineutron using the same machine. [9].

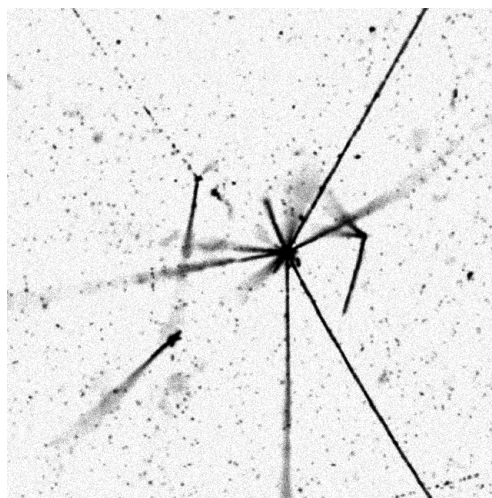


Figure 1.1: This image, taken from the  $AE\bar{g}IS$  collaboration site [1], shows the star shaped annihilation pattern caused by proton-antiproton annihilation.

Once the positron, antineutron, and antiproton had been found, scientists began to wonder if antimatter would come together to form antiatoms the way that matter came together to form atoms. In 1965, two separate groups detected antideuteron (an antiproton and an antineutron). One group, led by Antonino Zichichi, used the Proton Synchrotron at CERN in Geneva, Switzerland [10]. CERN, Conseil Européen pour la Recherche Nucléaire, is the world's premier particle physics facility. CERN is known today for the Large Hadron Collider, the best particle accelerator in the world. The other group, led by Leon Lederman, used a machine called the Alternating Gradient Synchrotron at the Brookhaven National Lab in New York, USA.

Next, scientists wanted to know if positrons could stick to antinuclei. In order to do this, they needed to slow down the antinuclei. CERN developed a new machine called Low Energy Antiproton Ring (LEAR), which actually slowed down the antinuclei before attempting to combine it with a positron. In 1995, a group at CERN successfully made nine antiatoms [11]. Hydrogen makes up three fourths of our universe. Could antihydrogen make up the majority of an antiuniverse? Does antihydrogen behave exactly like hydrogen? These were the next questions that faced the scientific community.

To investigate the properties of antihydrogen, CERN built the antiproton decelerator (AD). The AD is a storage ring for antiprotons. Antiprotons are created in the Proton Synchrotron by hitting metal target with a proton beam. These antiprotons are slowed down and held in the decelerator. The antiprotons are then fed into a different experimental apparatus.

Though the research questions have changed, antimatter remains a topic of interest to this day. According to Dirac's equations, there should be an equal amount of matter and antimatter in the universe. Additionally, modern high energy theory states that baryonic and leptonic numbers be

conserved. This requires a creation of an antiparticle for every particle and creation of a particle for every antiparticle. High energy physics experiments have confirmed that matter and antimatter are created in equal quantities up to a certainty of one part in  $10^{12}$  [12]. Obviously, our earth is made entirely of matter. So where is the antimatter? Dirac and others have proposed that there were large scale structures (galaxies or galactic clusters) made entirely of antimatter. However, astronomical observations have recorded only matter dominated structures. If large structures of antimatter existed, there would be a wall of radiation between the matter dominated universe and the antimatter dominated universe caused by annihilation of matter and antimatter. No such phenomena have been observed [13].

## 1.2 The role of $AE\bar{g}IS$ in the field of antimatter

$AE\bar{g}IS$  (Antimatter Experiment: Gravity, Interferometry, and Spectroscopy) is one of the four experiments that uses the antiproton decelerator (AD), a storage ring that produces low energy antiprotons, at Conseil European pour la Recherche Nuclaire (CERN).

$AE\bar{g}IS$  is designed to test the weak equivalence principle (WEP) for antimatter. This principle, a keystone of Einstein's relativity, states that all matter falls with the same acceleration. Physicists have tested this theory to a high precision for matter. It has never been directly tested for antimatter.  $AE\bar{g}IS$  must use cold antihydrogen (temperature  $O(\mu K)$ ) for the experiment. Charged particles such as antiprotons or positrons have interactions with electromagnetic fields that are much stronger than any deflection caused by gravity. This means that the test must be done with a neutral species, such as antihydrogen.

The antiprotons are injected into a  $AE\bar{g}IS$ 's apparatus and electric potentials are raised to contain the antimatter. There is also an axial magnetic field that, along with the electric potential, forms a device known as a Penning-Malmberg trap shown in Figure 1.2. It is comprised— as you can see in Figure 1.2— of a constant axial magnetic field and a pair of end voltages. In the Penning-Malmberg trap, two cylindrical end caps provide the voltages [3].

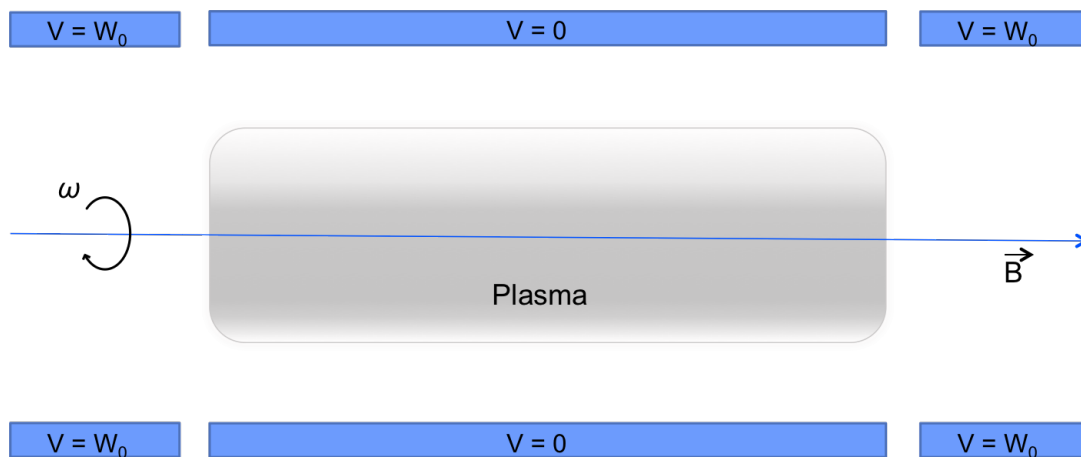


Figure 1.2: This is a schematic of a simple Penning-Malmberg trap. This is a trap designed to contain charged plasma. Two end voltages repel the charged particles in the center and an axial magnetic field gives radial confinement.

These are often used in plasma physics to contain non neutral plasmas, such as the positron plasma that  $AE\bar{g}IS$  has. The antiproton plasma in the  $AE\bar{g}IS$  trap is the target of the temperature measurement discussed in this thesis. We have developed a system on the  $AE\bar{g}IS$  apparatus to perform this measurement.

### 1.3 Temperature measurements for $AE\bar{g}IS$

Low temperatures are an important part of  $AE\bar{g}IS$ . The detector has a resolution limit ( $\approx 1\mu m$ ) [14]; in order for us to measure the acceleration caused by gravity, the average deflection (change in vertical position caused by acceleration due to Earth's gravitational field) of the antihydrogen must be greater than the detector's resolution limit. The deflection increases as the temperature decreases. This is because kinetic energy increases as temperature increases. A particle that is moving quickly in the direction perpendicular to earth's gravitational field has less time to fall towards earth as it traverses a given distance. This is demonstrated in Figure 1.3. This is why temperature is such an important aspect of the  $AE\bar{g}IS$  experiment.

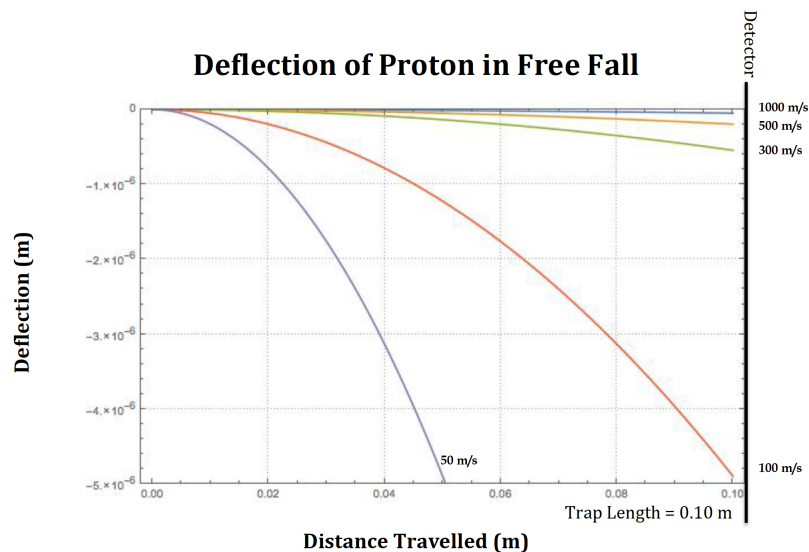


Figure 1.3: This graph demonstrates the distance in the vertical deflection of a proton falling in free fall on earth's surface. The slower the speed, the larger the deflection. Since the trap length is only 0.1 m and the detector resolution is limited, slower speeds are critical to ensure that particle deflection can be measured.

However, it is difficult to measure the temperature of an antimatter plasma because there is no way to apply a traditional, empirical method to an antimatter plasma. There is no thermometer that will not cause the antimatter to annihilate on contact. Thus, our method depends on kinematic theory and the concept that thermal kinetic energy of a particle is the same as the temperature.

## 1.4 Theoretical Motivation

Antimatter will allow us to test invariance under charge, parity, and time (CPT) reversal and the weak equivalence principle. In modern physics, particles and antiparticles are described by Relativistic Quantum Field Theory. A fundamental tenant of this theory is known as the CPT symmetry. This symmetry means that the laws of physics are symmetric under simultaneous transformations in charge, parity, and time reversal [15]. Current quantum field theories depend on CPT symmetry. The success of these theories and experiments on matter demonstrate the success of CPT symmetry. CPT symmetry demands that an antiparticle has the same mass,  $g$ -value, and lifetime as the particle. It has not been shown antiparticles have the same  $g$ -value as a particle. AE $\bar{g}$ IS will test CPT symmetry by looking at how antimatter falls in earth's gravitational field to see if the  $g$  value is indeed the same for matter and antimatter.

This is not the only way that antimatter is involved in CPT symmetry however. If the universe is in fact invariant under charge conjugation, parity transformation, and time reversal, there should be a mirror image for every particle. Physically, antimatter is this 'mirror image'. For CPT symmetry not to be violated, there should be exactly the same amount of matter and antimatter [16]. However, as far as current machines can detect, our universe is predominately matter.

## **Chapter 2**

# **Hardware for Temperature Calculation with AE $\bar{g}$ IS Apparatus**

## 2.1 Introduction and Background

The purpose of this chapter is to describe the hardware designed to take temperature measurements by  $AE\bar{g}IS$  at CERN.

The detectors designed for this measurement were added to the already existing  $AE\bar{g}IS$  apparatus. Before the measurement can begin,  $AE\bar{g}IS$  must receive the beam from the antiproton decelerator (AD). The antiprotons are injected into the  $AE\bar{g}IS$ 's apparatus and electric potentials are raised to contain the antimatter. There is also an axial magnetic field that, along with the electric potential, forms a Penning-Malmberg trap (Figure 1.1).

After capturing the antiprotons, we need to determine the energy of the particles one by one so that we can retrieve the temperature of the plasma. To this end, an apparatus was designed specifically to measure the temperature. The particles enter the apparatus from the main experiment and information about their position is output as a digital signal, which is then passed to the data acquisition system for  $AE\bar{g}IS$  where it joins all other experimental outputs. I will discuss the measurement apparatus in the order that a particle in the apparatus would come across the parts.

## 2.2 Description of the measurement apparatus

The apparatus is comprised of four elements: a 2 stage micro-channel plate detector (MCP detector), a phosphor screen, a front-end box, and a field programmable gate array (FPGA). The description is in the following sections.

### 2.2.1 Micro-channel plate detectors

Micro-channel plate (MCP) detectors are a class of detectors designed to count charged particles. The particle detected by the  $AE\bar{g}IS$  apparatus is an antiproton. MCP detectors are made of very small glass channels. The channels are surrounded by an electrode with a high resistance, typically 100-200 M $\Omega$ . Each channel acts as a separate electron multiplier tube. In the electron multiplier tube, each electron that enters interacts with a cathode and releases a shower of electrons, so that the detector emits more electrons than entered it. Figure 2.1 shows the orientation and binding of the MCP detector channels. The face is generally perpendicular to the incoming beam of particles (indicated by the arrow in Figure 2.1). The channels are placed at a small angle away from the horizontal, typically 7-9°, which increases the likelihood of a particle colliding with the capillary and initiating an electron shower.

$AE\bar{g}IS$  uses a two stage MCP detector. Essentially, two discs like the one in Figure 2.1 are placed one after another. There is a charge difference between the plates ( $AE\bar{g}IS$  uses 2V) to accelerate the electrons. The MCP detector plates are placed so that the capillaries are at opposing angles (this can be seen in Figure 2.2). The reason for this is that a two stage MCP detectors has greater signal amplification than one MCP detector alone can provide. A single MCP detector has gains around  $10^4$ , and a two stage MCP detector has gains on the order of  $10^6$ . However, there is more noise with two MCP detectors, which is offset by the front-end box later in the apparatus. The noise is self induced ion feedback. Since there is more volume inside the detector, there is more room for stray gas molecules to interact with the detector and create a false electron shower.

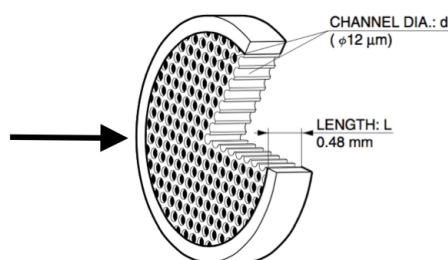


Figure 2.1: Diagram of a round MCP detector taken from the Hamamatsu Technical MCP Manual [2].

### 2.2.2 Phosphor Screen

A phosphor screen is a device that converts electrons into photons so that a visual image can be captured. The screen is created by coating a glass or fiber optic plate with a phosphor chemical. The phosphor molecules are densely packed. When an electron strikes the phosphor, the chemical releases light. This light can be imaged by a CCD camera. The phosphor de-excites over time and returns to its original un-illuminated state at which point, it can be used again.

The screen is placed after the two stage MCP detector, as you can see in Figure 2.2. Yet another voltage difference is applied to accelerate the electrons into the screen. Upon the collision of particles, the screen emits light proportionally to the number of electrons that impinge on it. The image on the screen can be up to 1,000,000 times brighter than the original image would have been.

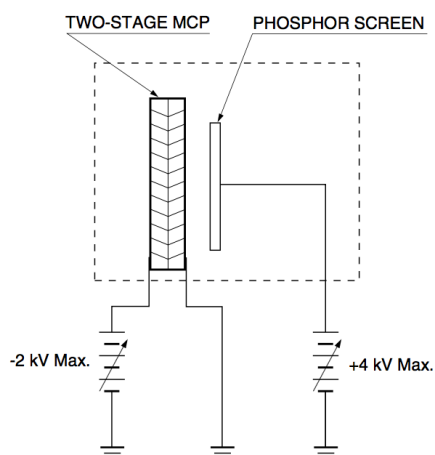


Figure 2.2: This image shows how the phosphor screen relates to the two-stage MCP detector. The two numbers -2kV and +4kV respectively show the strength of the relative voltage than can be applied. This diagram is taken from the Hamamatsu Technical MCP Manual [2].

### 2.2.3 Front-end Box

The front-end box serves several purposes. It is a box of different electronics designed to clean up the signal/image for processing. It couples the voltages from the high potential of the MCP detector and phosphor screen. This brings the signals to the same voltage for processing purposes.

It also has a field that works to counteract noise from the power supply, and it shapes the signal given by the MCP detector/phosphor screen. In any system, there is inherently something called dark noise, false detections that occur when there is no beam to measure. The two stage MCP detector has a higher dark noise than a single stage MCP detector, so it is important to offset this. The box removes signals that are weaker than a certain threshold, which differentiates between real and false signals. This effectively separates the dark current from the signal so that when the information leaves the box, it is clean and easier to work with than the unprocessed signal.

### 2.2.4 Field Programmable Gate Array

The field programmable gate array (FPGA) is a logic system that is designed to be configured for individual use by users and not by the supplier, hence the name ‘field programmable’. It is composed of thousands of hardwired logic blocks. Because it is hardwired, i.e. not programmed logic, it can make very rapid decisions.

One major function of the FPGA is to digitize the analog signal coming from the phosphor screen and the MCP detector. The FPGA logic gates break the signal down into small intervals (i.e. 10-20 particles, 20-30 particles, etc.) and record the digital signal in those intervals. The effect that this has on the signal is shown in Figure 2.3. This allows the signal to be passed to AE $\bar{g}$ IS’s data acquisition system to be processed by users on the AE $\bar{g}$ IS data analysis computers.

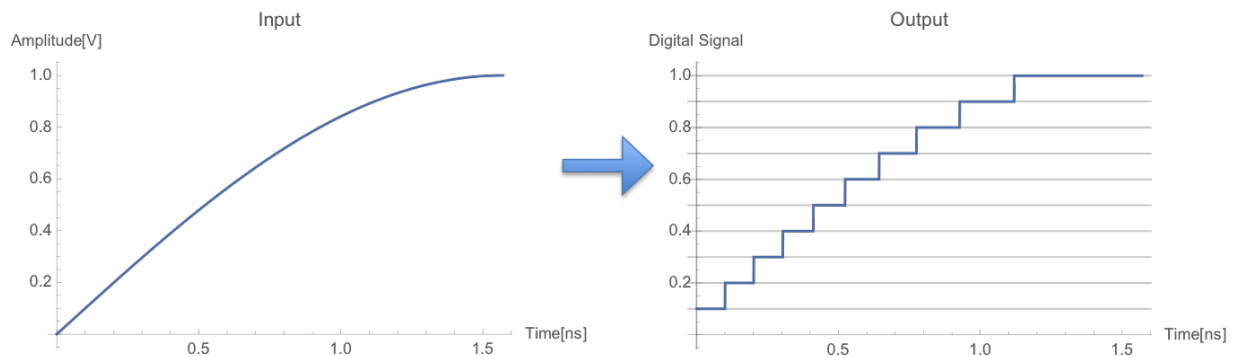


Figure 2.3: An example of an analog signal (left) being digitized (right).

## **Chapter 3**

# **Simulation of Plasma in the $AE\bar{g}IS$ Trap**

The goal of the code discussed here is to simulate a temperature measurement in the AE $\bar{g}$ IS apparatus and to see the effects of various parameters and sources of error.

### 3.1 Introduction and Basic Information

The code models a Penning-Malmberg trap, which is an electromagnetic configuration designed to contain charged particles. It has many applications in plasma physics and is necessary to contain antimatter in order to prevent annihilation of the antimatter with its surroundings. It is discussed in Chapter 1 and show in Figure 1.2.

We focus on the end potentials of the trap with our simulation as we create a 1-dimensional well that neglects the off-axis considerations of the magnetic field. The value of the potentials at the end must be high enough that no particle in the trap has sufficient energy to exit the trap. To achieve this, the walls are set at several times the potential needed to contain the most probable energy ( $E = 3/2k_bT$ ) where  $k_b$  is Boltzmann's constant and T is the temperature of the plasma [17]. For example, we chose ( $10k_bT/q$ ) where  $q$  is the charge of the particle ( $q = 1.602 \times 10^{-19}$  C) for all species considered (antiprotons, electrons, and positrons).

The number of particles input by the user are placed in the potential well. The number of particles in the simulation ranges between  $10^4 - 10^9$ . Of course, the number of particle numbers in the simulation can be set arbitrarily high, but the experiment has approximately the following particle numbers:  $\bar{p} \approx 2 \times 10^4$ ,  $e^- \leq 10^9$ , and  $e^+ \approx 10^7$ . For this reason, the particle number is constrained to  $< 10^9$ .

Next, the user decides the temperature at which the simulation will run. The value is typically chosen between 5 K and 50 K, but temperatures up to 1000 K have been explored. The AE $\bar{g}$ IS cryogenics system is designed to keep the system at cryogenic temperatures ( $\leq 50$  K). Using input temperature, the Maxwell-Boltzmann distribution is applied to the particles:

$$f(v) = \sqrt{\left(\frac{m}{2\pi k_b T}\right)^3} 4\pi v^2 e^{-\frac{mv^2}{2k_b T}} \quad (3.1)$$

Here  $f(v)$  is the number of particles at a given velocity,  $m$  is the mass of the particle, and  $v$  is the velocity of the particle [17]. This is based on the assumption that the particles in the trap are in thermal equilibrium. Particles in a Penning-Malmberg Trap rapidly reach thermal equilibrium [3]. The particles now move in the simulation with velocities determined by the Maxwell-Boltzmann distribution.

One end potential is lowered at a constant speed ( $\frac{\Delta W}{\Delta t}$ ), referred to as ramping speed, so that a voltage step of size  $\Delta W$  occurs every time interval  $\Delta t$  and a translation between time and voltage/energy can be made. This translation is key to our temperature calculation.

$$W_i = W_0 - i\Delta t \frac{\Delta W}{\Delta t} \quad (3.2)$$

where  $i$  is the step number,  $W_0$  is the initial potential, and  $W_i$  is the potential height at a given step. As the potential lowers, it eventually reaches a point where a particle has sufficient energy to escape  $E_{particle} \geq W_i q_{particle}$ . This particle is then counted in a histogram bin correlating to the step number in which it escaped. We continue to lower the potential and at each step the particles

that escape are counted. Note that only the particles in that step are counted; i.e., the counting is not cumulative. We then use the relationship between step number, bin, time, and voltage to retrieve the energy distribution and calculate the high energy tail of the Maxwell-Boltzmann distribution. An exponential fit, done with ROOT, provides the slope of the exponential curve of the particle per time histogram.

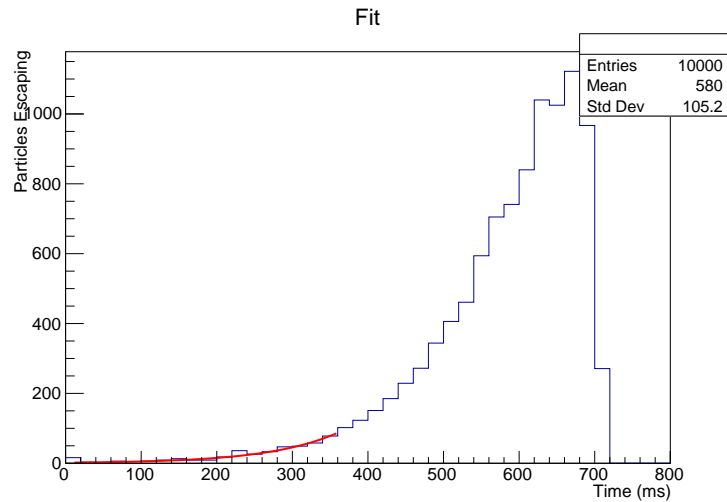


Figure 3.1: This a sample run, the red line shows the fit to the data.

Once the slope of the exponential plot is known, the temperature can be determined. To determine the temperature, the following equation is used:

$$T = \frac{q\Delta W}{mk_b\Delta t} \quad (3.3)$$

## 3.2 Parameter Space Explored

An important aspect of the temperature simulation code is its ability to allow users to explore experimental parameters without having to use time on the beam line. There are many parameters that affect the experiment: number of particles, voltage step size, and time step size to name a few. We can use this simulation to explore the parameter space to see what can cause errors in the fit.

Looking at the particle number, we see that with more particles we are able to achieve a higher resolution and better statistics which decreases the error. You can see this in Figure 3.2. The quality of the fit is better at  $10^5$  than at  $10^4$  particles.

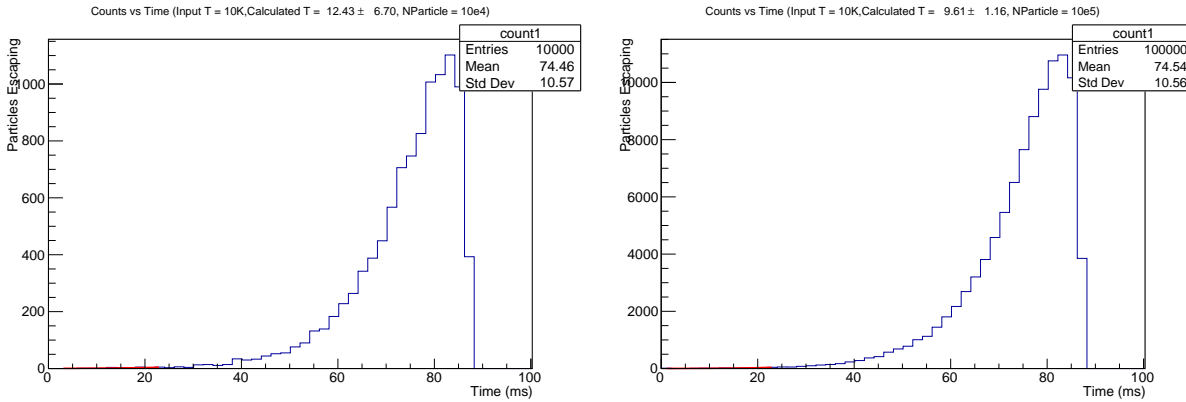


Figure 3.2: These plots have the same input parameters ( $T = 10$  K,  $\Delta W = 0.0001$  eV,  $\Delta T = 0.001$  K), except for the number of particles. You can see that the calculated temperature is closer to the real value and that the error is smaller for the higher particle number. The fit is shown by the small red line on the peak.

The values of  $\Delta W$  (voltage step) and  $\Delta t$  (time step) are defined separately because this affects the binning. For example, we often use  $\frac{\Delta W}{\Delta t} = 0.01$  but we could define  $\frac{\Delta W}{\Delta t}$  in many ways. For instance,  $\frac{\Delta W}{\Delta t} = \frac{0.1}{1} = \frac{0.0001}{0.001}$ . These definitions change the output. We see that the step size  $\Delta t$  determines the binning and hence the resolution. When  $\Delta t$  and  $\Delta W$  are  $\approx 1$  we have much lower resolution on the energy distribution and hence a higher error as you can see looking left to right in Figure 3.3 then when  $\Delta t$  and  $\Delta W \approx 0.1$ .

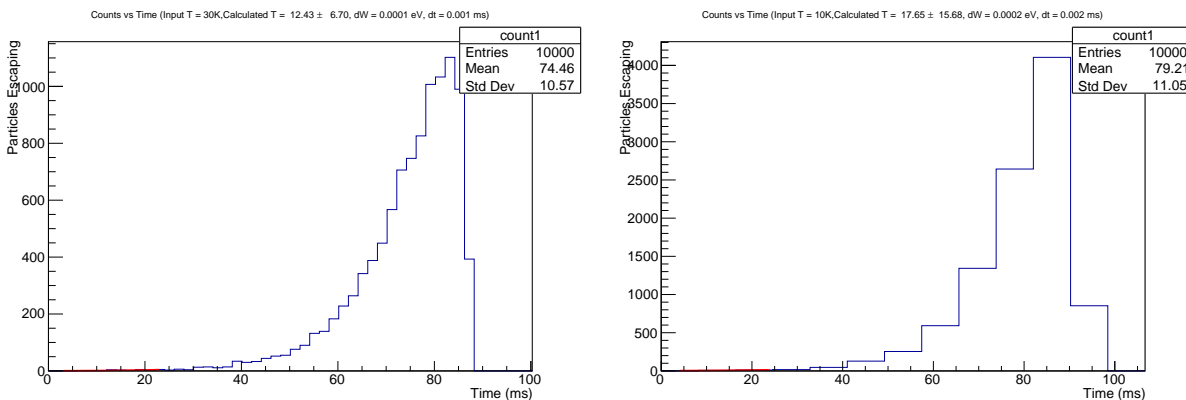


Figure 3.3: These graphs show the effects of the values of the potential steps  $\Delta W$  and the time steps  $\Delta t$ . You see looking from left to right that when you reduce the value of  $\Delta W$  and  $\Delta t$  by even  $1/4$  that you have a large change in the accuracy of the measurement. The small red line represents the fit to the 1% particles with the highest energy.

In addition to the size of the bins (i.e. the size of  $\Delta W$  and  $\Delta t$  separately), it is important to explore the value of the ramping speed ( $\frac{\Delta W}{\Delta t}$ ). The ramping speed determines the duration of the experiment. In [3], the author states that the ramping speed can be set arbitrarily high. However, we find that this is not the case, There is, in fact, a cap on the ramping speed, after which the fit is no longer reliable. This can be understood by carefully examining the process and recognizing

the importance of the step  $\rightarrow$  bin  $\rightarrow$  time  $\rightarrow$  energy translation. At each step ( $i$ ), the escaping particles have an energy  $E \geq qW_i$  and a finite speed  $v = \frac{\sqrt{E}}{m}$ . In order for the translation to occur successfully, all particles with this energy must escape the trap in that time step. If we consider a particle that is very near the end cap and has a negative velocity (it is moving away from the lowered potential), we see that it must travel a distance  $\approx 2L$  where  $L$  is the trap length, in the time window  $\Delta t$ . This provides a limiting speed.

$$2Lv \leq \Delta t \quad (3.4)$$

If the speed is higher than this, the particle will not escape in the allotted time and cannot be counted correctly.

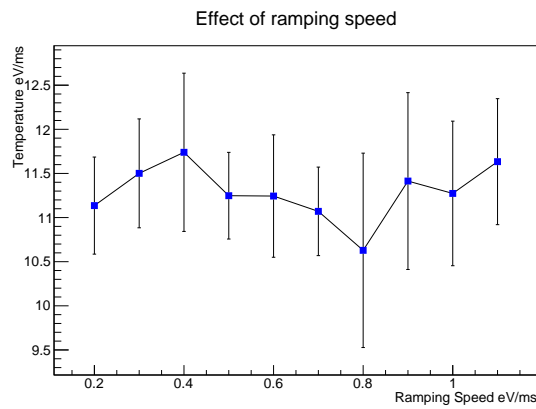


Figure 3.4: This image shows the calculated temperature as a function of ramping speed. In this case, the time step was held constant.

Figure 3.4 shows that the error increases as the speed increases. What it does not show, however, is that there is a speed at which the temperature can no longer be retrieved at all. The histogram is so incorrect that the fitting routine can no longer fit an exponential to it. This speed is  $v_{ramp} = 1.3 \pm 0.5$  eV/ms when the time step is 0.001 ms. Figure 3.5 shows an example of such a histogram.

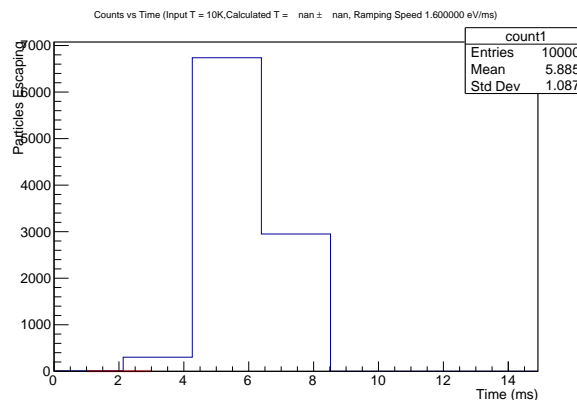


Figure 3.5: This is the example of a histogram for a ramping speed greater than  $1.3 \pm 0.5$  eV/ms.

We must also take care that the initial voltage  $W_0$  is sufficiently high to prevent any escaped particles at  $t = 0$ . If particles escape before the voltage is lowered, there are too many particles in the first bin and the fit is off. The mapping fails and can cause negative output temperatures. An example of a trap with an initial voltage that was too low is shown in Figure 3.6.

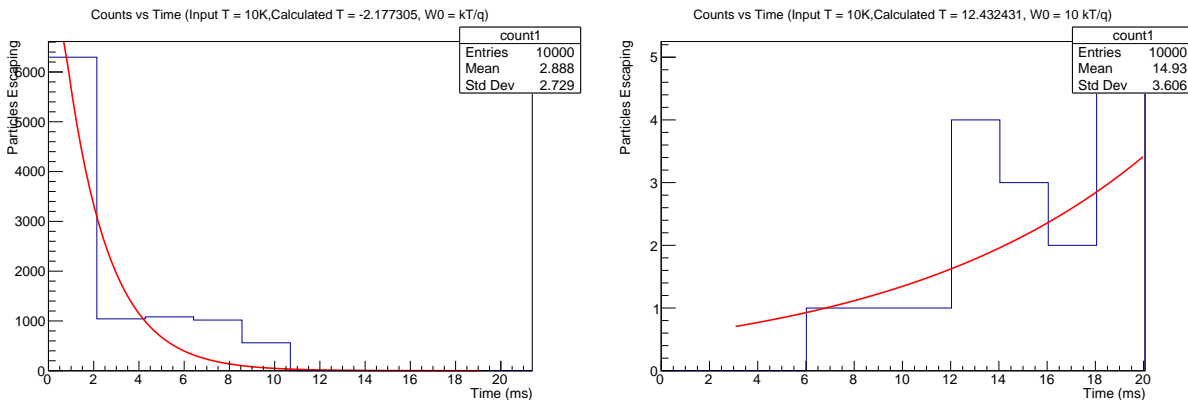


Figure 3.6: These figures are zoomed in so that you can see the high end tail of the fit. Note that in the left image, the first bin contains more particles than the second bin. This is because the potential well was set too low. As a result, the exponential fit is negative and gives a negative temperature. The right figure shows that changing the initial voltage changes the output temperature.

### 3.3 Error Analysis and Consistency Checks

The simulation outputs the absolute error on the calculated temperature. However, the error initially calculated is on the quality of the fit. The absolute error on the temperature must be calculated from this value. Using Equation (3.3), the absolute error of the temperature can be derived from the error on the slope of the fit. Equation 3.5 is used to calculate the absolute error on the calculated temperature.

$$\epsilon_T = \frac{T\epsilon_{fit}}{m} \quad (3.5)$$

Here,  $\epsilon_T$  and  $\epsilon_{fit}$  represent the absolute error on the temperature ( $T$ ) and the slope ( $m$ ) respectively.

We also considered noise on the electrode, which one may expect in an experimental setting. The electrode will not drop by exactly the same amount  $\Delta W$  every time. Sometimes it will drop slightly more than this and sometimes slightly less. To simulate this, a random number was added or subtracted to the average voltage step size. The error on the electrodes used by AEGIS is  $\pm 5 \times 10^{-5}$  V. Figure 3.7 shows how the noise on the hardware effects the measurement.

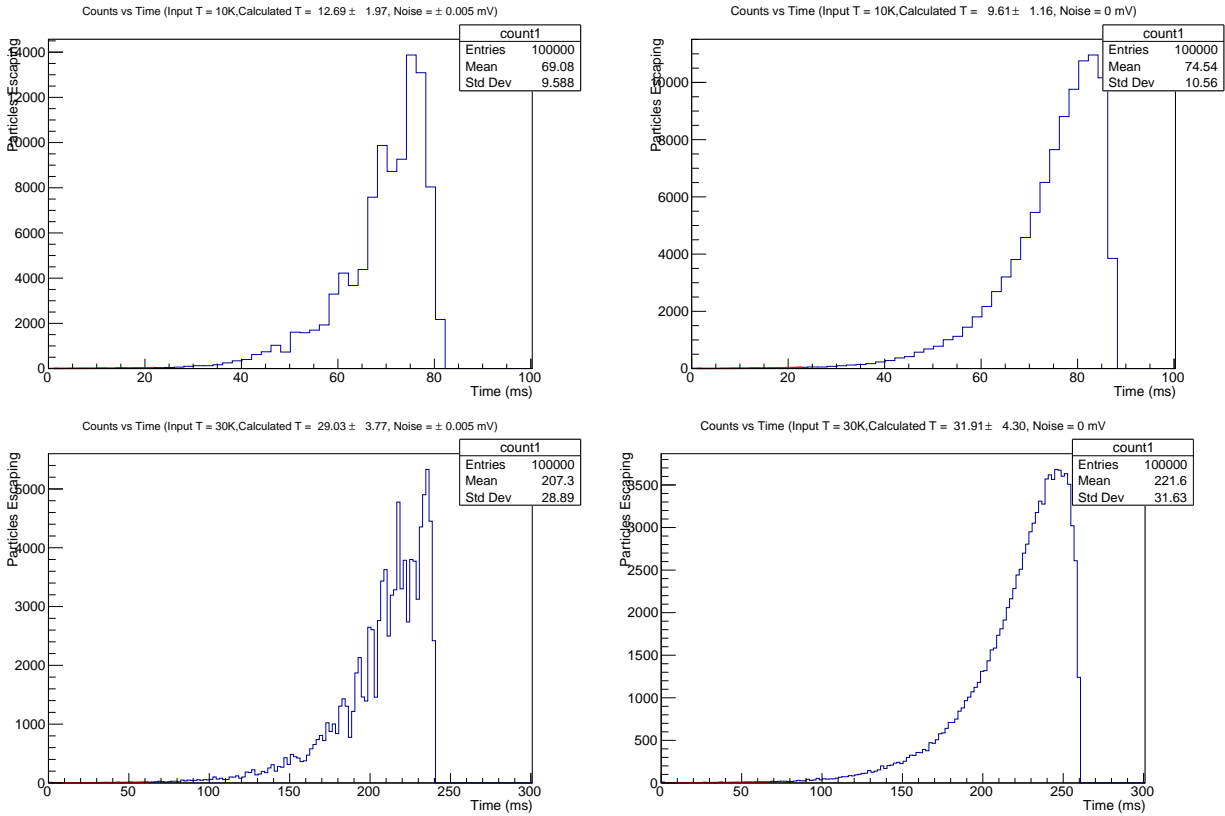


Figure 3.7: This figure shows how noise on the end caps that provide the voltages in the penning trap effect the measurement.

The code was also checked for self consistency. For instance, an experiment with a long trap length, the histogram will be distorted as particles fail to exit the trap in an appropriate time interval. So the effect of trap length on the shape of the histograms was explored. We also implemented a “detection efficiency” in the code to see if the simulation could mimic this aspect of the experiment. We have around 10% detection efficiency on the scintillators in the apparatus, so detection efficiencies down to that value were explored. Figure 3.8 shows the effects of detection efficiency on the temperature measurement at two different temperatures.

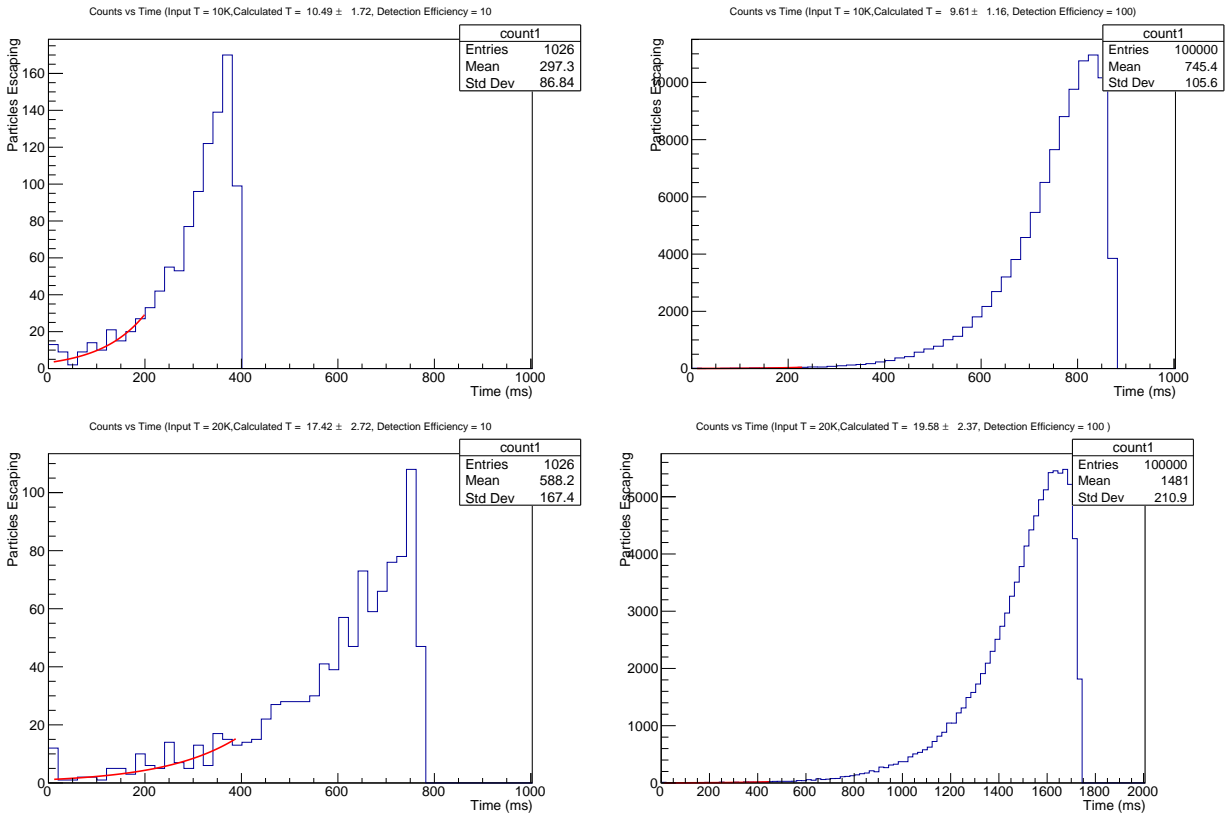


Figure 3.8: This figure contains four graphs that demonstrate the effect of detection efficiency on the temperature measurement. The two on the top have an initial temperature of 10 K and the bottom have an initial temperature of 20 K. On the left, the detection efficiency is set to 10% and on the right it is set to 100%. These plots demonstrate that the physical limitation of detection efficiency does not significantly affect the measurement.

This code is based on the work done in [3]. In order to calculate the number of particles that escape the trap, one must integrate over the Maxwell Boltzmann distribution. He gives the following approximation to the exact solution.

$$N \left[ \operatorname{erf} \left( \sqrt{\frac{W + dW}{k T}} \right) - \operatorname{erf} \left( \sqrt{\frac{W}{k T}} \right) \right] \approx N \left[ \operatorname{erf} \left( \sqrt{\frac{W}{k T}} \left( 1 + \frac{dW}{2W} \right) \right) - \operatorname{erf} \left( \sqrt{\frac{W}{k T}} \right) \right] \quad (3.6)$$

It is important to know the magnitude of the error for this approximation. I examined the percent error of the approximation. Setting up a simulation that used the full equation for one run and the approximation for the next run, the percent error from the approximation could be calculated. The results of the simulation are shown in Figure 3.9.

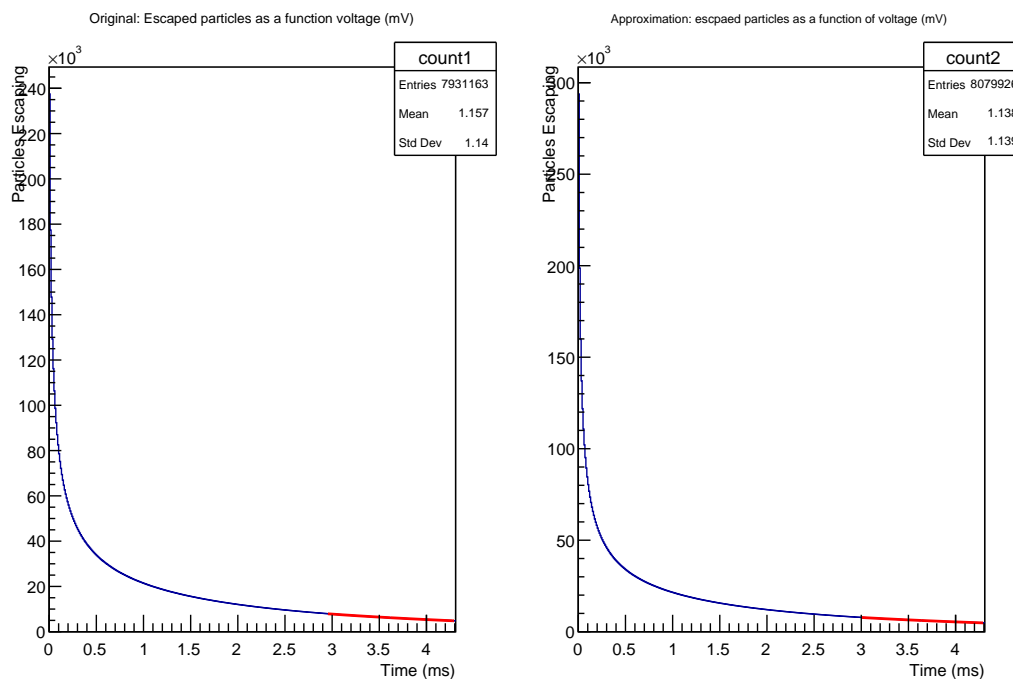


Figure 3.9: These are side by side plots where the original function and the approximated function have been used to determine how many particles escaped the trap. There is no visible difference in the two as the relative error is 0.0015% in this case ( $T = 50$  K).

Since the equation being approximated is a function of temperature and voltage, it was important to see how these variables affected the quality of the approximation. Figure 3.10 shows the percent error as a function of potential at different temperatures.

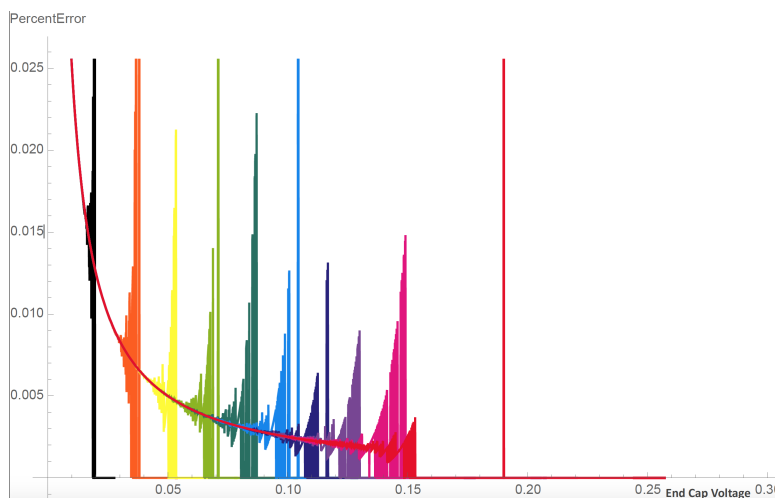
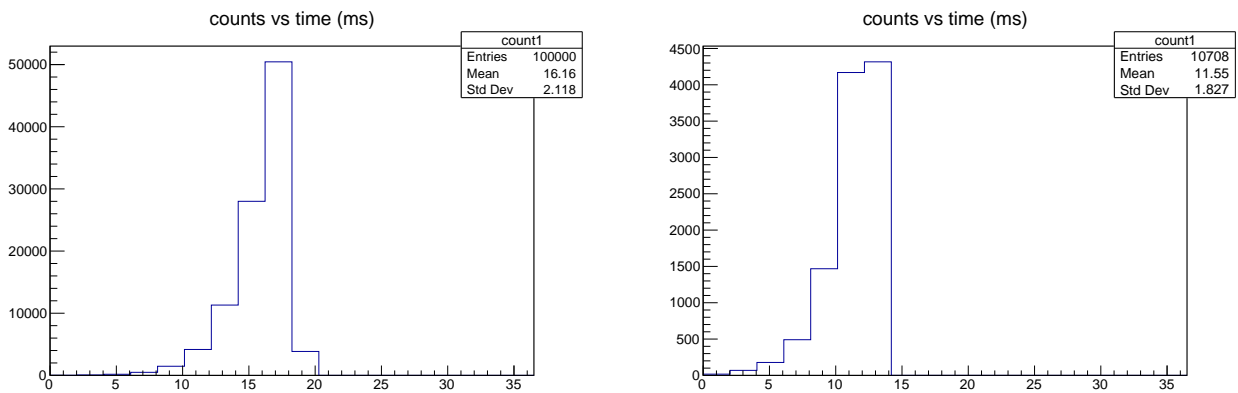


Figure 3.10: This shows the percent error on the number of escaped particles in a ramping step as a function of the voltage at the end cap. Each line corresponds to a different temperature from 10-100 K in increments of 10. The peak moves right as the temperature increases. However, the error in all cases is less than 0.025%, as you can see in this figure.

The approximation is worse at high temperatures and low voltages. However, this thesis is interested in the high voltage and low temperature regime. The error induced by the approximation in this regime is negligible.

For the trap length test there were two regions to explore. We have the region of “typical trap length” on the order of 0.1 m and a long trap length on the order of 1.0 m. In a long trap  $> 1$  m we expect to see two sets of exiting particles. We expect this because the first set of particles have a positive velocity, they are moving towards the lowered potential gate, and are able to escape. The second wave occurs as those who were moving away from the potential hit the opposite wall and turn around. We were unable to completely recreate this secondary peak. However, we were able to show that with a long trap length the first histogram has a modified shape as seen in Figure (3.11), which suggests that more particles are released at a later time in the anticipated second peak.



(a) This is the histogram for the regular length trap. All particles escape from the trap and the characteristic shape of the Maxwell Boltzmann velocity distribution is present.

(b) The trap in this simulation is 10x longer. It appears that the time taken is less than the time on the regular length trap, this is because particles may become stuck in the longer trap and not exit. Additionally, the shape of the distribution is distorted because the ramping speed is too fast to properly separate out the particles by energy for a trap this size.

Figure 3.11: The parameters used are as follows: particle number =  $10^5$ , temperature (T) = 20 K, Voltage steps (dW) = 0.001V, time steps (dt) = 0.001 s

### 3.4 Limitations on the model

Our simulation is limited in several ways. First, all quantum effects are neglected, treating the particles entirely classically. This assumption is especially inaccurate at low temperatures where quantum effects are larger. Recall that the particles are confined by magnetic fields. At very low temperatures, many particles are in their ground state. Positrons and electrons have spin, and quantum mechanically, they may align or anti-align with the magnetic field. This causes one ground energy to turn into two [18].

The space charge of the particles is also neglected. In a plasma, the total charge of the particles affects the dynamics. It effectively lowers the end potentials [19]. This can induce errors in the

binning because we only use the input voltage, not the effective voltage. This effect can be taken into account only in very complicated simulations. Figure (3.12) shows how the effective well depth  $W_{eff}$  changes as the applied potential  $W_0$  changes. The discrepancy between the two is caused by the space charge of the plasma.

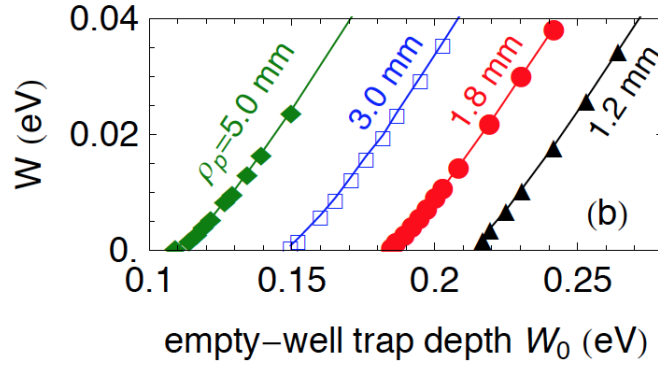


Figure 3.12: This figure is taken from [3]. This was made using a program known as EQUILSOR, which simulates plasmas. It shows calculation of the total trap depth  $W$  as a function of empty trap well depth  $W_0$  and density of the plasma  $\rho$

The space charge of the particles also affects the motion of the particles of the plasma. They exhibit collective motion as part of a plasma and their charge induces other plasma phenomena, but we neglect this.

### 3.5 Conclusions

This simulation demonstrates that the temperature of an antimatter plasma in a Penning Trap can be calculated within reasonable error based on measurement of particle energy. This simulation also allows helps narrow down acceptable parameter ranges, to reduce experiment time on the actual apparatus. Firstly, the code demonstrates that a potential as low as  $(10k_bT/q)$  is sufficient to contain the plasma and prevent error measurements. It is critical that the well be deep enough to contain all particles (see Figure 3.4), but we also want it to be as low as possible. Looking at Equation (3.2), it is obvious that the time taken to reach  $W_i = 0$ , when all the particles has escaped, depends on the initial potential heigh  $W_0$ . Due to this, it is valuable to know how low the initial voltage can reasonably be set.

Parameters such as number of particles, ramping speed, voltage step size, and time step size affect the success of the measurement. As one expects, the number of particles affects the quality of the fit. The smallest particle number that the AE $\bar{g}$ IS trap typically holds is  $\approx 10^4$ . The simulation shows that, while the results are better at higher particle numbers, the temperature can still be retrieved at this particle number. This simulation also explored the ramping speed on the potential and the step size for both voltage and time. It is demonstrated above that the step size, in addition to the speed, is important. Setting the ramping speed or the step size too large will induce error in the measurement. The ramping speed must remain below 1.3 eV/ms for time steps of 0.001 ms, or the temperature can no longer be retrieved. In order to make the simulation more realistic, the

detection efficiency was changed from 100% to 10%. The simulation demonstrates that while the error increased when the detection efficiency was lowered, the temperature could still be measured within reasonable certainty. Calculations were also done to test the validity of a mathematical approximation used to calculate the temperature. In the regime that AE $\bar{g}$ IS works ( $T < 50$  K) the error is less than 0.025%. These results demonstrate that the temperature calculation is analytically robust and can be implemented into AE $\bar{g}$ IS's analysis software. It also provides useful parameter constraints that will reduce the amount of time needed to actualize the temperature measurement on the apparatus.

## Chapter 4

### Outlook

The hardware discussed in this thesis has just been implemented on the  $AE\bar{g}IS$  apparatus. Preliminary measurements are being made to test the new hardware for any defects. An important next step is to take the calculation used to determine the temperature in the code and add it into gAn analysis framework. This will allow any  $AE\bar{g}IS$  user to determine the temperature of the plasma without having to do the calculation themselves.

Moving forward,  $AE\bar{g}IS$  will have a reliable way to determine the temperature of its antimatter particles. The current cryogenics system keeps the system below 50 K, but the experiment requires temperatures on the order of microkelvin. In order to achieve this, new cooling systems will be implemented.  $AE\bar{g}IS$  currently plans to use Sisyphus, Doppler, and evaporative cooling. In Sisyphus cooling, the particles move to a potential maximum, using up some of their kinetic energy, and a laser drops them to a lower energy state so that the potential energy is dissipated. This results in a lower kinetic energy and a lower temperature. Doppler cooling uses the doppler effect to tune lasers to particles moving towards the laser at a certain speed. The photons of the laser then impart their momenta on the particle which results in a frictional force as the momenta opposes the carbons motion. In evaporative cooling, the highest energy particles are excited, ionized and hence removed from the system. This lowers the net energy of the particles in the trap.

After the antiprotons are sufficiently cold, they can be combined with positrons to form antihydrogen. This process has been done successfully at higher temperatures than the ones  $AE\bar{g}IS$  will operate at. At this point,  $AE\bar{g}IS$  should be able to make measurements of the acceleration of antihydrogen caused by earth's gravitational field. The results of this cannot be anticipated. For matter, we have proven the weak equivalence principle; it remains to be seen whether this will be valid for antimatter.

# Bibliography

- [1] Aegis experiment: Testing gravity with antimatter at cern, 2014.
- [2] Electron Tube Division HAMAMATSU PHOTONICS K.K. Mcp assembly. Online, September 2006.
- [3] Philip John Richerme. *Trapped Antihydrogen in Its Ground State*. PhD thesis, Harvard University, May 2012.
- [4] Albert Einstein. Zur elektrodynamik bewegter körper. *Annalen der Physik*, 17, June 1905.
- [5] Rosy Mondardini. The history of antimatter.
- [6] Alaina G. Levine. Carl anderson, 2009.
- [7] This month in physics history, October 2006.
- [8] Owen Chamberlain, Emilio Segrè, Clyde Wiegand, and Thomas Ypsilantis. Observation of antiprotons. *Phys. Rev.*, 100, November 1956.
- [9] Bruce Cork, Glen R. Lambertson and Oreste Piccioni, and William A. Wenzel. Antineutrons produced from antiprotons in charge-exchange collisions. *Phys. Rev.*, 104, November 1956.
- [10] T. Massam, TH. Muller, B. Righini, M. Schneegans, and A. Zich. Experimental observations of antideuteron production. *IL NUOVO CIMENTO*, 39(1), September 1965.
- [11] Michael H. Holzschneider and. Antimatter gravity and antihydrogen production. *High Energy Physics*, September 1995.
- [12] K. Hagiwara et al. Review of particle properties. *Phys. Rev. D*, 66, July 2002.
- [13] Diego Casadei. Searches for cosmic antimatter. *Phys. Rev.*, 2006.
- [14] Mitsuhiro Kimura, S Aghion, O Ahlén, Claude Amsler, A Ariga, T Ariga, A Belov, Germano Bonomi, P Bräunig, J Bremer, R. Brusa, G Burghart, L Cabaret, Carlo Canali, Ruggero Caravita, Fabrizio Castelli, Giovanni Cerchiari, Simone Cialdi, Daniel Comparat, and S Zavatarelli. Development of nuclear emulsions with 1 m spatial resolution for the aegis experiment. *Nuclear Instruments and Methods in Physics*, 732:325, 01 2013.
- [15] Hilary Greaves and Teruji Thomas. The cpt theorem. *Mathematical Physics*, April 2012.

- [16] M. Villata. Cpt symmetry and antimatter gravity in general relativity. *A Letters Journal Exploring The Frontiers of Physics*, April 2011.
- [17] Charles Kittel and Herbert Kroemer. *Thermal Physics*. W. H. Freeman and Company, 2nd edition, 1980.
- [18] Ramesh Gopalan. *Studies of Cryogenic Electron Plasmas in Magnetic Mirror Fields*. PhD thesis, UNIVERSITY of CALIFORNIA at BERKELEY, 1998.
- [19] G. Gabrielse and X. Fei, L. A. Oroszco, and R. L. Tjoelker. Cooling and slowing of trapped antiprotons below 100 mev. *Phys. Rev.*, 63(13), September 1989.

## Academic Vitae

- Education**      Astronomy and Astrophysics      June 2014-Present  
Schreyer Honors College  
The Pennsylvania State University, University Park PA 16802
- Engineering Physics      Aug 2013-May 2014  
Lansing Community College  
4.0/4.0
- Experience**      Albert Einstein Institute      Max Planck Institute für Gravitation Physik  
Summer Student      May 2017- August 2017
- Determining geodesics and quasinormal modes for black holes with a Vaidya metric and a linear mass function in order to compare apparent and event horizons.
- Institute for Gravitation and the Cosmos      Pennsylvania State University  
Research Assistant      January 2017-May 2017
- Develop programs to determine the gravitational wave pattern of stellar mass compact object binaries with high spin.
- AEGIS Collaboration      CERN  
Research Assistant      June –December 2016
- Develop a ROOT simulation of the temperature measurement to be taken in the AEGIS beam line.
  - Working AEGIS beam control shift: communicating with beam control and other experiments, monitoring beam status, real time analysis and trouble shooting of the system, determining and controlling experimental variables
- Eracleous Laboratory      Pennsylvania State University  
Research Assistant      September 2014- Present
- Work on candidate supermassive binary black hole systems and line-emitting accretion disks in active galactic nuclei.
  - Develop scripts to drive programs that calculate the profiles of double-peaked emission lines. Then, simulate realistic spectra by adding synthetic noise.
  - Investigate how parameters (inclination angle, phase angle, etc.) of time-dependent perturbations, such as a spiral arm, affect the line profiles of disks.
- AEGIS Collaboration      CERN  
Research Assistant      1June –August 2015
- Work with mathematical descriptions of  $C_2^-$  in an penning trap with a magnetic mirror for sympathetic cooling of antiprotons used for gravity tests on anti-hydrogen
- Skills**      ROOT, C++, iOS, Microsoft Excel, Microsoft Word, Microsoft Powerpoint, Mathematica  
Python, Windows, Emacs, X-term (c shell), LaTeX, German (limited proficiency)
- Publications**      Runnoe, Jessie et al. (Feb 2017). *A Large Systematic Search for Close Supermassive Binary and Rapidly Recoiling Black Holes - III. Radial Velocity Variations.* *arXiv:1702.05465 [astro-ph.GA]*
- Presentations**      *Trapping and Cooling Antimatter for Gravity Research*      April 2016  
Schreyer Honors College: Scones and Scholarship

## Academic Vitae

	<i>Antimatter Research at CERN</i>	April 2016
	Graduate Women in Science: Spring 2016 Girl Scout Workshop	
	<i>Mathematical Descriptions of Axially Varying Penning Traps</i>	August 2015
	University of Michigan Research Experience, CERN	
<b>Posters</b>	<i>Temperature Measurement Simulation of Antiproton and Electron Plasmas for the AEGIS collaboration</i>	November 2016
	Physikerinnentagung 2016, DESY, Hamburg	
	<i>Can emission line profiles from perturbed accretion disks mimic those from the broad line region of a black hole in a supermassive binary?</i>	May 2016
	The Great Lake Quasar Symposium, Ontario, Canada.	
	<i>Can emission line profiles from perturbed accretion disks mimic those from the broad line region of a black hole in a supermassive binary?</i>	April 2016
	Pennsylvania State University Undergraduate Exhibition	
	<i>Can emission line profiles from perturbed accretion disks mimic those from the broad line region of a black hole in a supermassive binary?</i>	January 2016
	American Astronomical Society 227 <sup>th</sup> meeting	
	<i>Mathematical Descriptions of Axially Varying Penning Traps</i>	November 2015
	Out in Science, Technology, Engineering and Mathematics National Conference	
	<i>Mathematical Descriptions of Axially Varying Penning Traps</i>	July 2015
	Nonmember State Summer Student Program, CERN	
<b>Awards</b>	John and Elizabeth Holmes Teas Scholarship (36,000)	2017-2018
	Millennium Scholars Program (15,000\$ annually)	2014-Present
	Pennsylvania State University's Dean's List	2014-Present
	Academic Excellence Scholarship (4,500\$ annually)	2014-Present
	Provost Fund (2,000\$ annually)	2014-Present
	Beath Excellence Endowment (2,000\$ annually)	2014-Present
	Elsbach Honors Scholarship in Physics (2,500\$ annually)	2016-Present
	Braddock Homer Scholarship (5,000\$ annually)	2014-Present
	Erickson Discover Grant (3,400\$)	2016
	CERN Summer Student	2015
	George H Deike Scholarship (2,500\$ annually)	2015-2016
	Granville B. Lane Memorial Scholarship (2,500\$ annually)	2015-2016
	Gerald L Bayles Memorial Scholarship (2,500\$ annually)	2015-2016
	Lansing Community College Dean's List	2013-2014
	Schumacher Honors Scholarship (2,500\$ annually)	2014
<b>Organizations</b>	American Physical Society	2015-Present
	American Astronomical Society	2015-Present
	Sigma Pi Sigma Physics Honors Society	2016-Present
	The Honors Society of Phi Kappa Phi	2016-Present
	National Society of Leadership and Success	2015-Present